

Southern Methodist University

SMU Scholar

Electrical Engineering Theses and Dissertations

Electrical Engineering

Summer 2022

Empirical Models of 3D Air-to-Air Communication Channels

Neil Matson

ncameronmatson@gmail.com

Follow this and additional works at: https://scholar.smu.edu/engineering_electrical_etds



Part of the [Systems and Communications Commons](#)

Recommended Citation

Matson, Neil, "Empirical Models of 3D Air-to-Air Communication Channels" (2022). *Electrical Engineering Theses and Dissertations*. 53.

https://scholar.smu.edu/engineering_electrical_etds/53

This Thesis is brought to you for free and open access by the Electrical Engineering at SMU Scholar. It has been accepted for inclusion in Electrical Engineering Theses and Dissertations by an authorized administrator of SMU Scholar. For more information, please visit <http://digitalrepository.smu.edu>.

EMPIRICAL MODELS OF 3D AIR-TO-AIR COMMUNICATION CHANNELS

Approved by:

Joseph D. Camp
Electrical and Computer Engineering
Thesis Committee Chairperson

Dinesh Rajan
Electrical and Computer Engineering

Prasanna Rangarajan
Electrical and Computer Engineering

EMPIRICAL MODELS OF 3D AIR-TO-AIR COMMUNICATION CHANNELS

A Thesis Presented to the Graduate Faculty of the

Lyle School of Engineering

Southern Methodist University

in

Partial Fulfillment of the Requirements

for the degree of

Master of Science in Electrical Engineering

by

Neil Cameron Matson

B.S., Electrical Engineering, Southern Methodist University, 2017

August 3, 2022

Copyright (2022)

Neil Cameron Matson

All Rights Reserved

Matson, Neil Cameron B.S., Electrical Engineering, Southern Methodist University, 2017

Empirical Models of 3D Air-to-Air Communication Channels

Advisor: Joseph D. Camp

Master of Science in Electrical Engineering conferred August 3, 2022

Dissertation completed June 1, 2022

Unmanned Aerial Vehicles (UAVs) often lack the size, weight, and power to support large antenna arrays or a large number of radio chains. Despite such limitations, emerging applications that require the use of swarms, where UAVs form a pattern and coordinate towards a common goal, must have the capability to transmit in any direction in three-dimensional (3D) space from moment to moment. In this work, we design a measurement study to evaluate the role of antenna polarization diversity on UAV systems communicating in arbitrary 3D space. To do so, we construct flight patterns where one transmitting UAV is hovering at a high altitude (80 m) and a receiving UAV hovers at 114 different positions that span 3D space at a radial distance of approximately 20 m along equally-spaced elevation and azimuth angles. To understand the role of diverse antenna polarizations, both UAVs have a horizontally-mounted antenna and a vertically-mounted antenna—each attached to a dedicated radio chain—creating four wireless channels. Using the data from this channel-sounding experiment we are able to estimate the air-to-air (A2A) channel and build a model of the channel for arbitrary azimuth and elevation angles. We use this model to analyze the effect antenna orientation and UAV relative position have on channel magnitude. First, we quantify the different ways in which the UAV body can alter the radiation pattern of a dipole antenna depending on whether the antenna is perpendicular or parallel to the body of the UAV. Then, we analyze the effect the change in the radiation pattern has on the cross-polarization discrimination (XPD). Finally, we calculate the overlapping index, a distance measure, between the distribution of channel magnitude in two symmetric regions of 3D space

and observe that the two distributions are further apart when the receiver (Rx) is below the transmitter (Tx), suggesting an asymmetry in the way the Tx and Rx UAV body affect the channel. To demonstrate the impact these effects could have on communication systems, we compute the average throughput at each location based on the channel estimates, show how to optimally select an antenna orientation, and quantify the gains in such selections.

TABLE OF CONTENTS

LIST OF FIGURES	viii
LIST OF TABLES	x
ACKNOWLEDGMENTS	xi
CHAPTER	
1. Introduction	1
1.1. Related Work	2
2. In-field Measurement Campaign	4
2.1. UAV Channel Sounding Platform	4
2.2. Coordinate Systems	4
2.2.1. UAV-Based	4
2.2.2. Antenna-Based	5
2.3. Flight Plan Design and Experimental Procedure	6
2.4. Data Extraction	7
2.4.1. Flight Log	7
2.4.2. USRP IQ Samples	8
3. System Model and Channel Metrics	10
3.1. Channel Estimation	10
3.2. Metrics	11
3.2.1. Antenna Radiation Pattern	11
3.2.2. Cross-Polarization Discrimination	12
3.2.3. Capacity	12
4. Campaign Results and Analysis of A2A Channels	13
4.1. Quantifying UAV Flight Plan Accuracy	13

4.1.1. Transmitter Position	13
4.1.2. Receiver Position	15
4.2. Impact of Antenna Orientation	15
4.2.1. Impact of UAV-Antenna Orientation on Radiation Pattern	16
4.2.2. Impact of UAV-Antenna Orientation on XPD	17
4.3. Asymmetric impact of UAV body in 3D Space	20
4.4. Effect of Position and Antenna Orientation on Capacity	24
4.4.1. Fixed Antenna Orientations	24
4.4.2. Best Antenna Pair	25
5. Conclusions	28
BIBLIOGRAPHY	30

LIST OF FIGURES

Figure	Page
2.1. UAV Chanel Sounding Platform	5
2.2. (a) The global, UAV based coordinate system defining the relative position of Rx UAV to the Tx. (b) Orientation of the UAV body and the location of the co- and cross-polarized antennas in the Tx antenna based coordinate systems for UAV orientation 1 (the plane of the UAV body is perpendicular to the Tx antenna.) (c) The same for UAV orientation 2 (the long side of UAV body is parallel to the Tx antenna.) The notch represents the top, front of the UAV.	5
2.3. Envelope of the one receiver antenna’s IQ Data along with identified waypoints from IMU synchronization.	9
3.1. Received signal \mathbf{Y} and estimated signal $\hat{\mathbf{Y}}$ after performing least-squares estimation of the channel \mathbf{H}	11
4.1. Mean plus-or-minus one standard deviation of (a) TX and (b) RX UAV position displacement from intended at azimuth angle $\phi = 0$ and each elevation angle, θ	14
4.2. Interpolated channel magnitude over 3D space of (a) the C2 (HH) channel in the global, UAV based coordinate system, (b) the same channel expressed in the Tx antenna based coordinate system, (c) the C1 (VV) channel. The differences between (b) and (c) are due to the UAV body blocking the link at azimuth angles around 0° and 180° . Marked lines as plotted in polar coordinates in Fig. 4.3	16
4.3. Magnitude of the channel between the co-polarized antennas with different body orientations as described in Table 2.1. (left) Variation over azimuth at 0° elevation angle. (right) Variation over elevation angle at azimuth angles 0° and 90° . When the UAV body is parallel with the Tx antenna (C2), the body blocks the LoS path at certain azimuth angles, e.g. 0° . . .	18

4.4. Magnitude of the channels between co- and cross-polarized antennas over the azimuth angle for (left) perpendicular and (right) parallel UAV body scenarios as illustrated in Fig. 2.2. The perpendicular UAV body causes polarization mixing, reducing XPD, while the parallel body causes the XPD to vary significantly over the azimuth angle. 19

4.5. Estimated density functions $\hat{f}(|h|^2)$ of the C1 (VV) channel magnitude $|h|^2$ in the front and behind hemispheres at elevation angles (a) $\theta = -30.5^\circ$ (b) $\theta = 43.5^\circ$ and (c) $\theta = 10^\circ$ estimated via Eq. 4.1. The overlap index in (a), (b), and (c) are $\eta = 0.124, 0.411,$ and $0.809,$ respectively, which in turn correspond to the minimum η when Rx is below, the minimum η when the Rx is above, and maximum η over all elevation angles. 22

4.6. Average channel magnitude ($\pm\sigma$) of the of the C1 (VV) channel over azimuth angles where the Rx UAV is in front of or behind the Tx UAV at different UAV based elevation angles θ^G . The value of η is the percentage of overlap between the estimated “in front” and “behind” densities. $\eta = 1$ indicates that the pdf of the two distributions are equal. 23

4.7. Average capacity of the (a) VV and (b) HH TX-RX antenna pairs. 25

4.8. (a) Average capacity of the HV and (b) and VH TX-RX antenna pairs. 26

4.9. (a) Best performing TX-RX antenna pair and (b) its capacity. 27

4.10. Distribution of measured capacity over 3D space of four fixed TX-RX pairs and ”best-pair” selection strategy. 27

LIST OF TABLES

Table	Page
2.1. Naming Conventions in UAV and Tx Antenna Based Coordinate Systems . . .	6
4.1. Std. Dev. of Co-Polarized Channel over Elevation Angle	18
4.2. XPD Statistics over Azimuth Angle ϕ	20

ACKNOWLEDGMENTS

I would like to thank my advisors Dr. Camp and Dr. Rajan for their guidance and advice; all of my colleagues and peers from my time at SMU, especially Hashir and Sicheng for their invaluable contributions to this work particularly the experiment design and data collection; and finally, my friends and family for supporting me during this process and always. This work would not have been possible without each of them, and for that, I am forever grateful.

Chapter 1

Introduction

Unmanned aerial vehicles (UAVs) have received a lot of interest in recent years. There seems to be no end to the number of news stories promising that these small, flying robots will change the world. But it isn't just media hype. Advances in flight control, improvement in battery efficiency, and increases in computing power have made UAVs an attractive platform to be used in a variety of applications. There have been real examples of UAVs helping first responders in search-and-rescue missions [1] and using UAVs to deliver life-saving medication to people located in places typical distribution routes cannot reach [2]. Most relevant to this thesis, however, is the promise of UAVs to extend and add new capabilities to wireless communication networks, particularly through the use of multiple UAVs. Fleets of UAVs carrying radio hardware can be used to set up ad-hoc networks to respond to unexpected outages, like those resulting from natural disasters [3] or increased demand due to large events [4].

The placement of traditional wireless communication infrastructure must be carefully planned because once the equipment installed, it is static. Additionally, traditional wireless networks are typically modeled as existing in a two-dimensional (2D) plane. The promise of UAVs is to use their mobility to bring the wireless coverage to where it is needed, in *three-dimensional* (3D) space. But with these extra degrees of freedom come new challenges. Where should the UAV be to provide the best wireless performance to a user on the ground? To multiple users? How should multiple UAVs coordinate to achieve these goals? What types of antennas and signalling should be used? Where should the antenna be placed on the UAV? All of these are of course questions that are asked of traditional wireless systems, but for a new platform like the UAV, we need new answers.

To build practical wireless systems and networks, both theoretical and experimental research is needed. One can start with the physics of the radio signals and model how those

electromagnetic waves interact with the environment. But the models that describe those interactions are typically based, or at least verified, on measurements from the physical world. Simulation is a powerful tool when planning a system, but the accuracy of the simulation will only be as good as the underlying model, which should be the product of sound theory and rigorous empirical data.

This thesis presents the results of in-field measurement campaign to quantify the impact of antenna orientation and placement and arbitrary 3D UAV location on the air-to-air (A2A) channel between two UAVs. We perform channel sounding measurements of four distinct channels based on antenna orientation by flying two UAVs through a comprehensive flight plan, covering all angles in 3D space. Our analysis demonstrates the importance of understanding the relationship between the antenna orientation and where the two UAVs are in relation to one another. We quantify how the orientation of the antenna, with respect to the UAV body, can significantly alter antenna characteristics like radiation pattern and cross-polarization discrimination (XPD). Our measurements also show that there are asymmetries between the probability distribution of the channel magnitude different regions of 3D space— asymmetries that are unexpected for usually symmetric vertical dipole antennas and arise due to the interaction between the antenna and the UAV body. We finally demonstrate the impact that these effects can have on communication by estimating the throughput of the UAV-to-UAV connection from our channel measurements. These results suggest that with one radio chain and two antennas, the UAVs can maintain a stable throughput regardless of their relative locations, something that is unachievable with a single antenna.

1.1 Related Work

A number of prior works have simulated drone networks, often focusing on the flight dynamics and modeling with simplifying assumptions for UAV connectivity [5, 6].

There have been a number of recent UAV channel measurement studies; see the surveys [7, 8]. These works represent a wide variety of UAV experiments (different types of aircraft, varying degrees of mobility, and multiple environments,) but of the majority of these works, e.g. [9–20] consider only the air-to-ground (A2G) channel. In each of the studies, the authors investigate how some of the unique aspects of communication systems involving UAVs affect

the wireless channel. For example, some [9, 10] investigate the effect of airframe shadowing on the channel. Others [11–14] observe the impact of the relative elevation angle between the UAV and the ground station. The type of antenna used and how it is mounted on the UAV can be a determining factor in how much the airframe or elevation angle affects the channel. Multiple antenna orientations are explored in [15–20].

Likely because of the inherent challenges of controlling multiple UAV platforms in flight, there have been far fewer campaigns to measure the air-to-air (A2A) channel [19–23]. These studies have either involved small aerial sensors [20–22], or only considered a limited number of angles in 3D space [19, 23]. Previous research conducted at SMU [24, 25] has investigated the effect of antenna orientation and placement on the A2A wireless channel for a limited number of azimuth and elevation angles. By contrast this work represents a complete 3D view of the air-to-air channel conducted under real-world conditions.

Chapter 2

In-field Measurement Campaign

2.1 UAV Channel Sounding Platform

To measure the A2A channel in 3D space, we fly two UAVs simultaneously; one acting as a transmitter (Tx) and one as a receiver (Rx). Each UAV, a DJI Matrice 100, is outfitted with an Ettus USRP E312 software-defined radio attached via a custom 3D-printed mount. The E312 has two independent RF chains that can function in either Tx or Rx modes. The RF chains share a local-oscillator and are phase aligned. The E312 is also equipped with Inertial Measurement Unit (IMU) to capture orientation information which is used to align the wireless data with the UAV GPS location (see Section 2.4).

We attach two antennas to the Tx/Rx ports of the E312 at the front of the UAV. One antenna is mounted vertically (V) such that the length of the antenna is perpendicular to the body of the UAV and sticks out above the landing legs and propellers. The other antenna is attached horizontally (H), sticking straight out from the front of the UAV. The horizontal antenna lies in the same plane as the UAV body and legs. The antennas (VERT2450 from Ettus) are omni-directional dipole antennas with 3 dBi gain. The UAV platform is shown in Figure 2.1. Note that the Tx and Rx configurations are identical.

2.2 Coordinate Systems

2.2.1 UAV-Based

We use a spherical coordinate system, as shown in Fig. 2.2a, to define the position of the Rx UAV with respect to the Tx UAV. The underlying right-handed Cartesian coordinate system is oriented such that the positive x-, y-, and z-axes point East, North, and Up, respectively, with the Tx UAV at the origin. The global, UAV based (to distinguish for the later defined local, Tx antenna based) azimuth angle $\phi^G \in [0, 360)$ is measured clockwise in

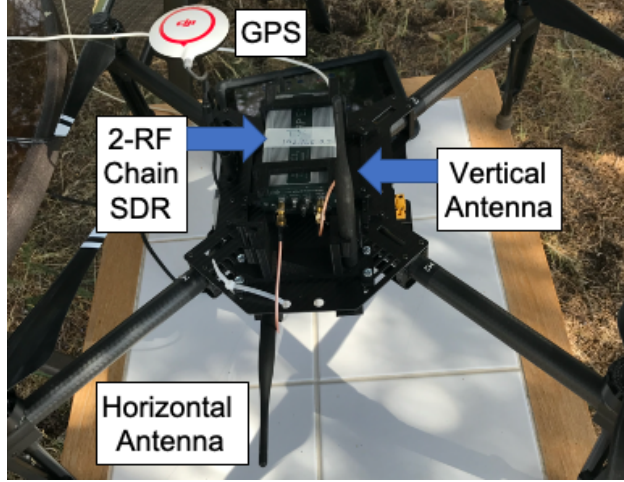


Figure 2.1: UAV Channel Sounding Platform

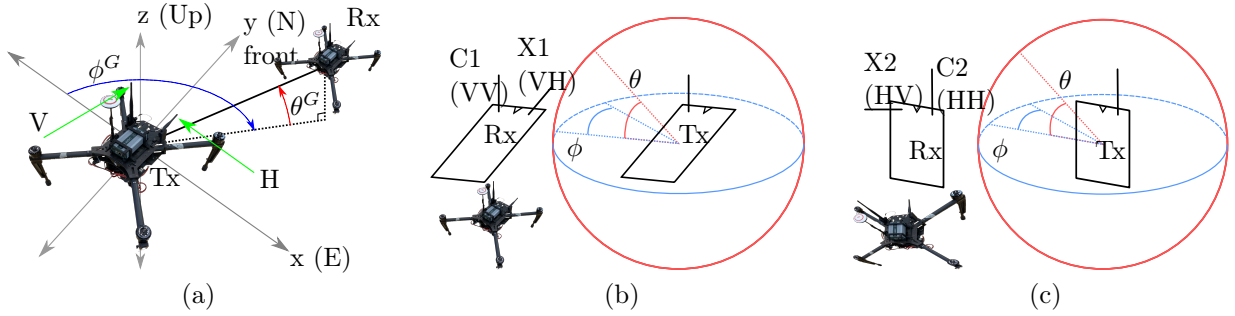


Figure 2.2: (a) The global, UAV based coordinate system defining the relative position of Rx UAV to the Tx. (b) Orientation of the UAV body and the location of the co- and cross-polarized antennas in the Tx antenna based coordinate systems for UAV orientation 1 (the plane of the UAV body is perpendicular to the Tx antenna.) (c) The same for UAV orientation 2 (the long side of UAV body is parallel to the Tx antenna.) The notch represents the top, front of the UAV.

the xy -plane from the negative x -axis (due West); similarly the elevation angle $\theta^G \in [-90, 90]$ is defined as the angle above or below the xy -plane.

2.2.2 Antenna-Based

When quantifying the impact that the UAV body/antenna orientation has on the channel magnitude and antenna parameters (e.g. the radiation pattern and XPD which will be further defined later) at a particular point in 3D space, we define the azimuth and elevation

Table 2.1: Naming Conventions in UAV and Tx Antenna Based Coordinate Systems

UAV based	Polarization and Body Orientation	Tx based
VV	Co-pol Perpendicular	C1
VH	X-pol Perpendicular	X1
HH	Co-pol Parallel	C2
HV	X-pol Parallel	X2

angles, ϕ and θ , to be the location of the Rx antenna relative to the *vertical* orientation of the Tx antenna. For the vertically mounted antenna, we directly have $\phi = \phi^G$ and $\theta = \theta^G$. In order to define antenna-based coordinate system for the horizontally Tx mounted antenna, however, we utilize a transformation that rotates the entire coordinate system by 90° such that the rotated positive z-axis is aligned with the horizontal antenna. We refer to this as the “Tx antenna based coordinate system” because, regardless of whether or not we are referring to the vertically or horizontally mounted antenna on the drone in the experiment, the Tx antenna is *always* vertical in the coordinate system during analysis. Therefore, in addition to referring to the channels by the antenna pair orientation with respect to the UAV (i.e., VV, VH, HV, or HH), we will also describe the four channels as C1, X1, C2, and X2, respectively, to represent the co-polarized (C) or cross-polarized (X) channel in two separate scenarios which we call Perpendicular (1) and Parallel (2) in reference to the orientation of the UAV body with respect to the Tx antenna. The equivalent naming conventions for the UAV based and Tx antenna based coordinate systems are summarized in Table 2.1. Fig. 2.2b and Fig. 2.2c show the UAV and antenna configuration of C1, X1 and C2, X2 channel in their Tx antenna based coordinate systems, respectively.

2.3 Flight Plan Design and Experimental Procedure

Recall that the location of the transmit drone, which hovers 80 m above the ground, is defined as the origin of the spherical coordinate system used to define the position of the Rx UAV. In our experiment, the receiver drone hovers at fixed locations around the transmitter in 3D space at a radial distance of roughly 20 m. These locations are defined by an angle pair (ϕ, θ) . The azimuth angle, ϕ , is measured clockwise from the West axis and varies between

0° and 360°. The elevation angle, θ , is defined as the angle above or below parallel (both drones at same height) and varies between -90° (receiver is directly below the transmitter) and 90° (receiver is directly above the transmitter). We take measurements over 16 azimuth and nine elevation angles at intervals of 22.5° for a total of 114 unique locations spanning 3D space (Note that at locations directly above or below, $\theta = \pm 90^\circ$, the azimuth angle ϕ is undefined).

To reliably control the position of the receiver drone, the spherical coordinates (ϕ, θ) are translated into GPS coordinates (longitude, latitude, elevation) using the MATLAB Mapping Toolbox, exported to a keyhole-markup-language (.kml) file, and uploaded to the DJI GSPRO flight planner tool. Flight time is limited by the capacity of the drone battery; therefore, measurements are taken over eight flights consisting of 16 locations each. During each flight, the receiver begins at $\theta = -90^\circ$ and flies in a vertical circle around the transmitter, hovering for 20 seconds at each elevation angle. Both UAVs always face North during the experiment.

Both SDRs are programmed via GNURadio using the USRP Hardware Driver and operate at a 200 kHz sample rate. From take-off until landing, the Tx continuously transmits two independent signals from each of its two antennas. The signals are sent over a 2.484 GHz carrier frequency. This frequency is the 802.11 (WiFi) channel 14 which is unused in the United States (where this experiment took place) and free of interference. Likewise, the Rx continuously records the received IQ samples from each antenna.

2.4 Data Extraction

2.4.1 Flight Log

The DJI GSPRO flight planner tool records flight data such as speed, GPS coordinates, and IMU readings continuously throughout the duration of the flight, but the log does not indicate the waypoints from the flight plan; therefore, we need a method for identifying which samples correspond to each measurement location. To identify waypoint locations, we compute a simple metric $g_{\text{UAV}}(t)$ that captures the combined effect of the roll $r_{\text{UAV}}(t)$ and pitch $p_{\text{UAV}}(t)$ components of the IMU sensor as follows:

$$g_{\text{UAV}}(t) = \sqrt{r_{\text{UAV}}^2(t) + p_{\text{UAV}}^2(t)}. \quad (2.1)$$

We then perform peak-finding on g_{UAV} . We assume that at the midpoint in time between two peaks, the receiver is midway through its 20-second hover. From this timestamp, we isolate a 1-second window centered at the midpoint to analyze the receiver position.

2.4.2 USRP IQ Samples

In addition to the flight log timestamps, we also have the start and stop time of the IQ data recording. Unfortunately, because of the separate processors of the UAV and USRP, we have two notions of time, and thus need a method to align the two data sets. We do so by utilizing the IMU sensors of both the USRP and UAV. We compute $g_{\text{USRP}}(t)$ from $r_{\text{USRP}}(t)$ and $p_{\text{USRP}}(t)$ as in (2.1). We perform peak-finding on g_{USRP} . Then, to align the two IMU signals, we calculate the delay between the first peak in $g_{\text{UAV}}(t)$ (which corresponds to takeoff) and the nearest peak in $g_{\text{USRP}}(t)$ and apply this delay to the appropriate time signal.

We now have the same notion of time for the USRP and UAV signals, which along with the known sampling rates of each, allows us to match samples from the UAV flight log and the measured IQ data from the USRP. We repeat this process for each flight. Once the IQ samples have been matched to the corresponding azimuth and elevation angles of each measurement location, we analyze the wireless channels using the procedure described in Section 3.

Fig. 2.3 shows $g_{\text{USRP}}(t)$, the envelope of the IQ data for one of the receiver channels for one flight, and the identified waypoints. The samples corresponding to the measurement waypoint are then saved for further processing.

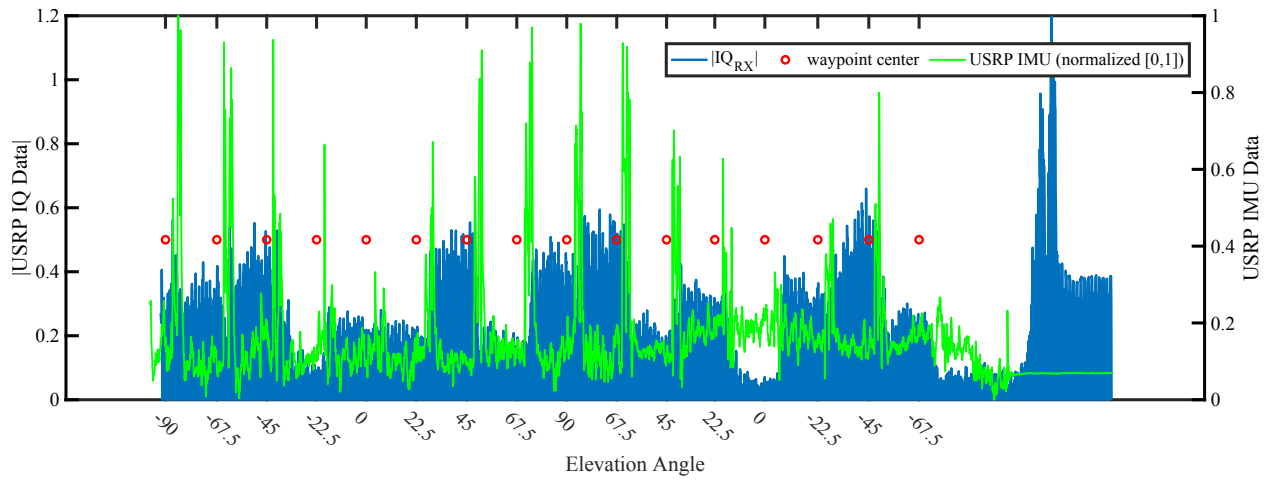


Figure 2.3: Envelope of the one receiver antenna's IQ Data along with identified waypoints from IMU synchronization.

Chapter 3
System Model and Channel Metrics

In order to estimate the channels of the four distinct antenna pairs, we model the discrete-time the 2x2 A2A channel as:

$$\underbrace{\begin{bmatrix} y_V(n) \\ y_H(n) \end{bmatrix}}_{\mathbf{y}(n)} = \underbrace{\begin{bmatrix} h_{VV} & h_{HV} \\ h_{HV} & h_{HH} \end{bmatrix}}_{\mathbf{H}} \underbrace{\begin{bmatrix} x_V(n) \\ x_H(n) \end{bmatrix}}_{\mathbf{x}(n)} + \underbrace{\begin{bmatrix} z_V(n) \\ z_H(n) \end{bmatrix}}_{\mathbf{z}(n)}$$

Where $x_i(n), y_i(n), z_i(n)$ are the transmitted signal, received signal, and effective noise on antenna $i \in \{V, H\}$ at time instance n , and h_{ij} is the complex-valued SISO channel between Tx antenna i and Rx antenna j . We are thus able to measure four distinct channels: a co-polarized (VV, HH) and a cross-polarized (VH, HV) for each antenna orientation.

3.1 Channel Estimation

In our experiments, we transmit a fixed, complex sinusoid at different frequencies from the two transmit antennas. These tones allow us to estimate all four channels in \mathbf{H} simultaneously. Specifically, we set $x_H(n) = 0.7e^{j2\pi f_1 n}$ and $x_V(n) = 0.7e^{j2\pi f_2 n}$ where f_1 and f_2 were selected as 5 kHz and 15 kHz, respectively, and n represents the time-index. The value of 0.7 is an arbitrary scale factor to prevent clipping at the Tx. To estimate the channel, we compute the least squares estimate $\hat{\mathbf{H}}$ of the channel using a finite number of signal samples:

$$\hat{\mathbf{H}} = (\mathbf{X}^\dagger \mathbf{X})^{-1} \mathbf{X}^\dagger \mathbf{Y}, \quad (3.1)$$

where \mathbf{X} is $2 \times N$ shaped matrix consisting of N consecutive, non-overlapping samples of the transmit signal, \mathbf{Y} is a similarly shaped matrix of output samples, and \mathbf{X}^\dagger is the conjugate transpose of \mathbf{X} . For each of the N samples, a single estimate of the channel is obtained. We experimentally consider different values for N but only show the results for $N=50$ samples as

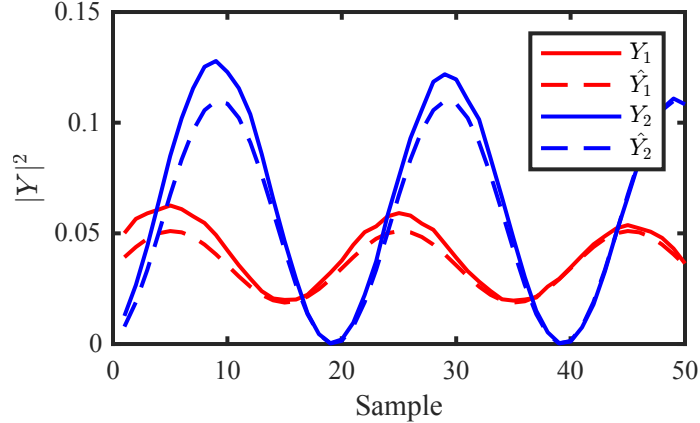


Figure 3.1: Received signal \mathbf{Y} and estimated signal $\hat{\mathbf{Y}}$ after performing least-squares estimation of the channel \mathbf{H} .

it allows for low mean-squared-error over the segment without over-fitting. This corresponds to a channel coherence time of $250 \mu s$. An example of the result of channel estimation is shown in Fig. 3.1 which depicts the measured signal at each Rx antenna \mathbf{Y} and the estimate of this signal, $\hat{\mathbf{Y}}$, after estimating the channel $\hat{\mathbf{H}}$. The entire processing of the RX USRP data to obtain the channel estimate is conducted in MATLAB.

3.2 Metrics

In this work, we primarily analyze the magnitude of the SISO channels, $|h|^2$, and quantify how it is affected by the orientation of the UAV body and relative position of the UAVs. We compare the measured channel magnitude to that of the theoretical channel based on the following quantities:

3.2.1 Antenna Radiation Pattern

The magnitude of the channel is proportional to the pathloss¹, which is a function of the product of the gains, or radiation patterns, of the Tx and Rx antennas, G_T and G_R . The theoretical radiation pattern of a vertical (oriented along the positive z-axis) dipole antenna is $G_V(\phi, \theta) = \cos(\theta)$ [26]. Note that the pattern does not depend on the azimuth angle ϕ and varies from its maximum value at $\theta = 0^\circ$ to 0 at $\theta = \pm 90^\circ$. The magnitude of

¹We consider only the large-scale free-space pathloss as the experiment takes place in an open LoS environment at a sufficient altitude to avoid ground based multipath.

the channel between the co-polarized vertical antennas is thus proportional to $G_V G_V$, i.e., $|h_{VV}|^2 \propto G_V(\phi, \theta) G_V(\phi, \theta) = \cos^2(\theta)$.

3.2.2 Cross-Polarization Discrimination

The cross-polarization discrimination (XPD) is the difference (in dB) in the received power between a co- and cross-polarized antenna pair. In a slight abuse of terminology, we define it here to be the difference in the channel magnitudes of the same. For example, for a vertically oriented Tx antenna, we have $XPD_{V,dB} = 10 \log(|h_{VV}|^2) - 10 \log(|h_{VH}|^2)$. In theory, the channel magnitude between a vertical Tx antenna and horizontal Rx antenna (or vice-versa) should be extremely low, resulting in low cross-polarized received power compared to the co-polarized, thus the XPD would be very high.

3.2.3 Capacity

In addition comparing the channel magnitude directly, we use capacity to quantify the quality of each of the four wireless channels in $\hat{\mathbf{H}}$. For example, the capacity per unit bandwidth of the channel h_{VV} can be calculated as [27]:

$$C_{VV} = \log_2\left(1 + \frac{P}{N_o} h_{VV}^2\right) \quad (3.2)$$

In (3.2), P/N_o is the signal (P) to noise (N_o) ratio (SNR) at the vertical receiver antenna element. For simplicity, we normalize the SNR by setting $P=1$ and measuring the effective noise power N_o at the receiver when there is no transmit signal. Similarly, we calculate the capacity of the h_{VH} , h_{HV} and h_{HH} channels using (3.2).

Chapter 4

Campaign Results and Analysis of A2A Channels

We now turn to the analysis of the A2A channel. First, we will provide a analysis of the UAV flight behaviors. Then, we will look at the effect of antenna orientation, relative to the UAV body, on the A2A channel by comparing the channel magnitude as well as the cross-polarization discrimination. Next, we will analyze how the relative location of the Rx UAV with respect to the Tx UAV can impact the channel. And finally, we will look at the estimated throughput for each of the four antenna pairings.

4.1 Quantifying UAV Flight Plan Accuracy

We suspect one reason for the lack of in-field, air-to-air channel measurements is the difficulty of simultaneously flying multiple UAVs accurately and precisely. There are many variables such as GPS inaccuracies, wind, and drone vibrations within a single flying system, let alone two, especially over several flights. We have observed this in our previous work [25]. We would like to be able to control these variables as much as possible, but when we cannot control them completely, we would like to quantify them to observe their effects.

In this study, we seek to measure the channel at a receiver drone located at distinct azimuth and elevation angles from a transmitter drone. To this end, we quantify how accurately those azimuth and elevation angles are reproduced in the experiment. We the present absolute position of both the transmitter and receiver to demonstrate that their positions are stable when hovering. Then we discuss their relative position, i.e. the angular separation between the two drones, and show that our experiment uniformly samples locations over the 3D space around the transmitter.

4.1.1 Transmitter Position

Fig. 4.1a shows the transmit drone’s average displacement (Δ) from the intended location based on the UAV GPS data for each of the eight flights. There is a small variation in the

mean positions between the flights; however, since the variation is less than a meter, the mean positions can be treated effectively the same. Further, the standard deviation within each flight suggests how much the transmitter drone moved as it hovered in place. The average deviation in the displacement across all flights was only 80 mm, which indicates that the transmitter was effectively stationary.

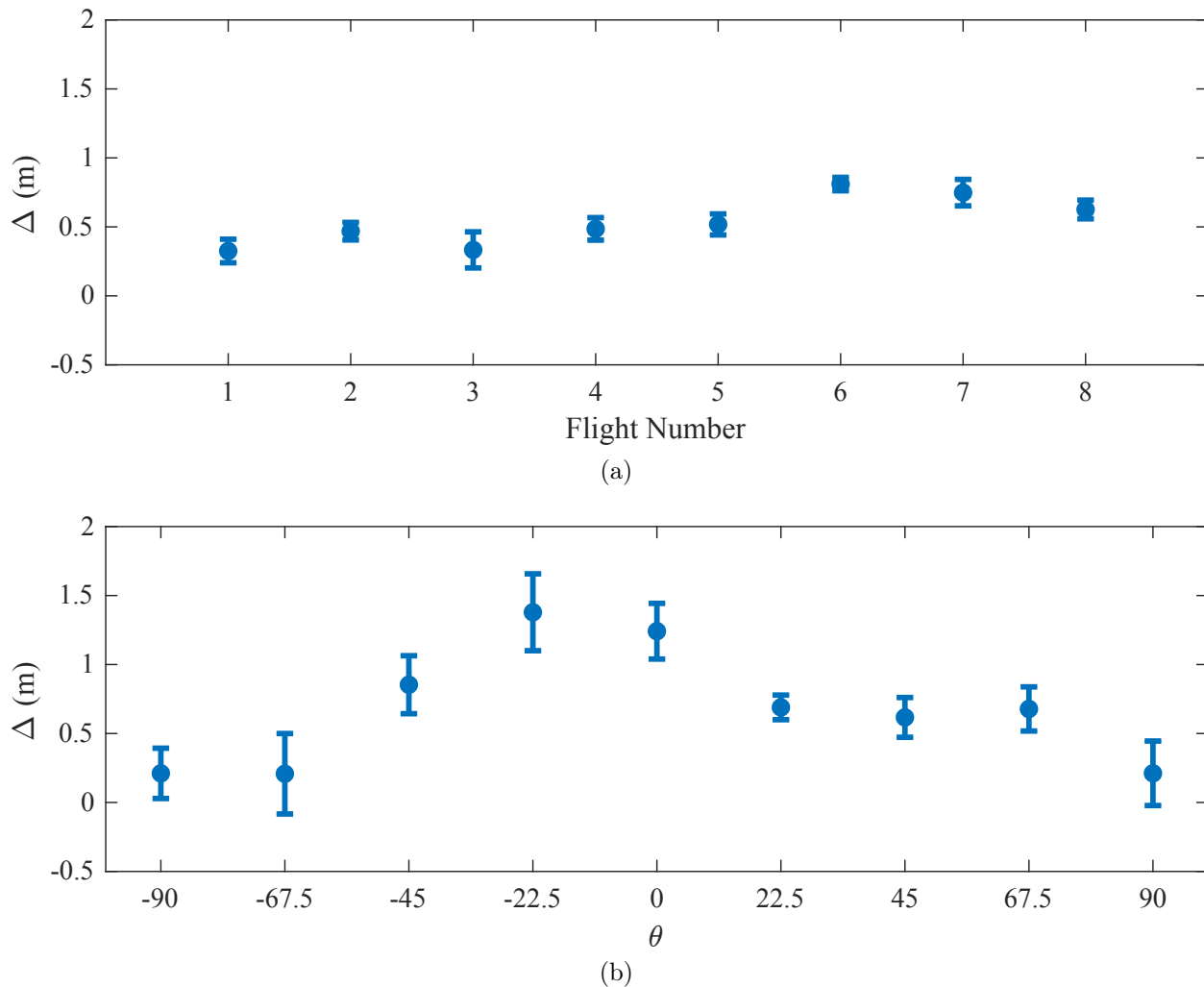


Figure 4.1: Mean plus-or-minus one standard deviation of (a) TX and (b) RX UAV position displacement from intended at azimuth angle $\phi = 0$ and each elevation angle, θ .

4.1.2 Receiver Position

For the receiver, we partition each flight log in a similar manner as the one described in Section 2.4.2. As with the transmitter, we want to ensure that the receiver UAV is close to its intended location and is stable at that location for each waypoint along the flight. As an example, consider Fig. 4.1b, which shows the average displacement from the intended location for each elevation angle when the azimuth angle was equal to 0. While the average displacement of the receiver is higher than that of the transmitter, it is relatively small compared to the separation distance between the transmitter and receiver of 20 m. Again, what is more important is the standard deviation. Across all measurement locations, the average standard deviation of displacement from the intended receiver location was 161 mm suggesting that the receiver’s position was stable.

We have shown that the transmitter and receiver are effectively stationary at each of the measurement locations; however, there are some absolute position errors. A reasonable question is whether or not those errors affect the ability of the study to capture the A2A channel over all angles in 3D space. As it turns out, the positional errors are small enough relative to the drone separation distance that each of the (ϕ, θ) pairs are still spaced approximately uniformly.

To emphasize this, the datapoints in the figures in Section 4.4 are centered at the actual measured location data rather than the locations corresponding to the intended angles. Though there are slight offsets from the grid of the “globe”, the measured locations effectively cover the entire space.

4.2 Impact of Antenna Orientation

We now show the ways in which the relationship between the UAV bodies and antennas can affect the A2A channel. We first analyze the impact of the orientation UAV body on the radiation pattern over the azimuth and elevation angles. Then, we quantify how the orientation affects the cross-polarization discrimination for different antenna orientations. Lastly, we present how the UAV body can cause asymmetries in the distribution of the channel magnitude in symmetrical hemispheres by blocking or reflecting the signal depending on the relative UAV positions.

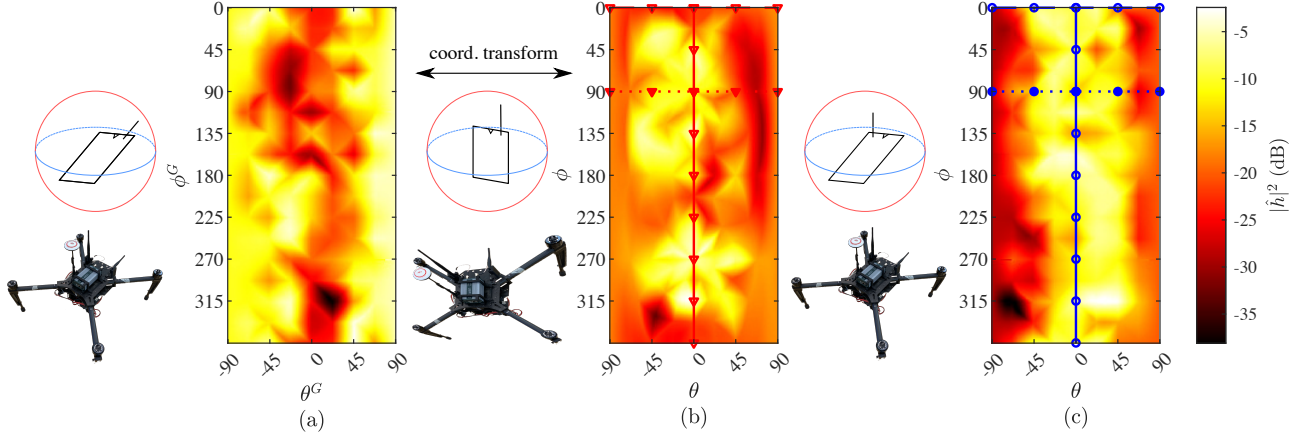


Figure 4.2: Interpolated channel magnitude over 3D space of (a) the C2 (HH) channel in the global, UAV based coordinate system, (b) the same channel expressed in the Tx antenna based coordinate system, (c) the C1 (VV) channel. The differences between (b) and (c) are due to the UAV body blocking the link at azimuth angles around 0° and 180° . Marked lines as plotted in polar coordinates in Fig. 4.3

Our dataset consists of 114 unique locations spaced at 22.5° intervals over the azimuth and elevation angles. In order to compare arbitrary angles in both the original and rotated coordinate systems as defined in Section 2.2, we perform a 3D scattered interpolation on each dataset. We first calculate a Delaunay Triangulation to generate a 2D surface in 3D space and then do natural-neighbor interpolation on each triangle at 0.5° spacing. This interpolation guarantees C^1 continuity [28].

4.2.1 Impact of UAV-Antenna Orientation on Radiation Pattern

Fig. 4.2 shows 2D representations of the interpolated channel magnitude estimates $|\hat{h}|^2$ over all azimuth and elevation angles, along with a cartoon of the UAV body and antenna configuration of both the Tx and Rx (as described in Section 2.2) for that channel. The marked lines in (b) and (c) correspond to particular fixed values of azimuth and elevation angles which are plotted in polar coordinates in Fig. 4.3.

Fig. 4.2(a) and (b) both show the C2 channel (co-polarized link, UAV bodies *parallel* to Tx antenna, i.e. HH) in the UAV and Tx antenna based coordinate systems, respectively, while Fig. 4.2(c) shows the C1 channel (co-polarized link, UAV bodies *perpendicular* to Tx antenna, i.e. VV). The C1 channel behaves similarly to the theoretical radiation pattern of

a vertical dipole antenna, i.e. it is strongest at small elevation angles, weak at large elevation angles, and shows little dependence on the azimuth angle. One might expect the C2 channel to behave similarly since, theoretically, the radiation pattern is the same. Indeed, Fig. 4.2(b) shows that the channel is strongest at small values of θ and weakest at large values; however, the channel is clearly not independent of the azimuth angle, ϕ . At low elevation angles, the channel is significantly weaker at azimuth angles near 0° or 180° .

The reason for this decrease in the channel magnitude is that, at these azimuth angles, the UAV body blocks the line-of-sight path between the two antennas. This blockage only occurs in the parallel UAV body scenario because the antennas lie in the plane of the UAV body and legs, while the perpendicularly mounted antennas stick up above them.

Fig. 4.3 shows “slices” of both the C1 and C2 channel magnitudes as they vary over azimuth angle ϕ (left) and elevation angle θ (right). The C1 channel varies much less with ϕ than the C2 channel. The standard deviation of the C1 channel at $\theta = 0^\circ$ over ϕ is 2.7 dB, approximately half as much as that of the equivalent C2 channel at 5.2 dB. Additionally, the UAV body can reduce the magnitude of the C2 channel by up to 12 dB compared to the magnitude of the C1 channel at the same azimuth angle.

The orientation of the UAV body also effects the elevation angle dependence of the channel. Fig. 4.3(b) shows the channel magnitude vs. elevation angle of the C1 and C2 channels at two azimuth angles, $\phi = 0^\circ, 90^\circ$. The path between the Tx and Rx for both C1 channels as well as the C2 channel at $\phi = 90^\circ$ is mostly LoS, and the channel magnitude behaves similarly to the expected radiation pattern, i.e., strong at $\theta = 0^\circ$ and decreasing towards $\theta = \pm 90^\circ$. The LoS path of the C2 channel at $\phi = 0^\circ$, however, is blocked by the UAV body regardless of the elevation angle. This channel is, therefore, generally weaker than the other three and does not vary as much with θ . The standard deviation for each of these four scenarios is given in Table 4.1.

4.2.2 Impact of UAV-Antenna Orientation on XPD

In addition to affecting the radiation pattern, the UAV body produces local scattering of the signal which can cause polarization mixing, reducing the XPD. Fig. 4.4 shows the channel magnitude of both the co- and cross-polarized channels over all azimuth angles at

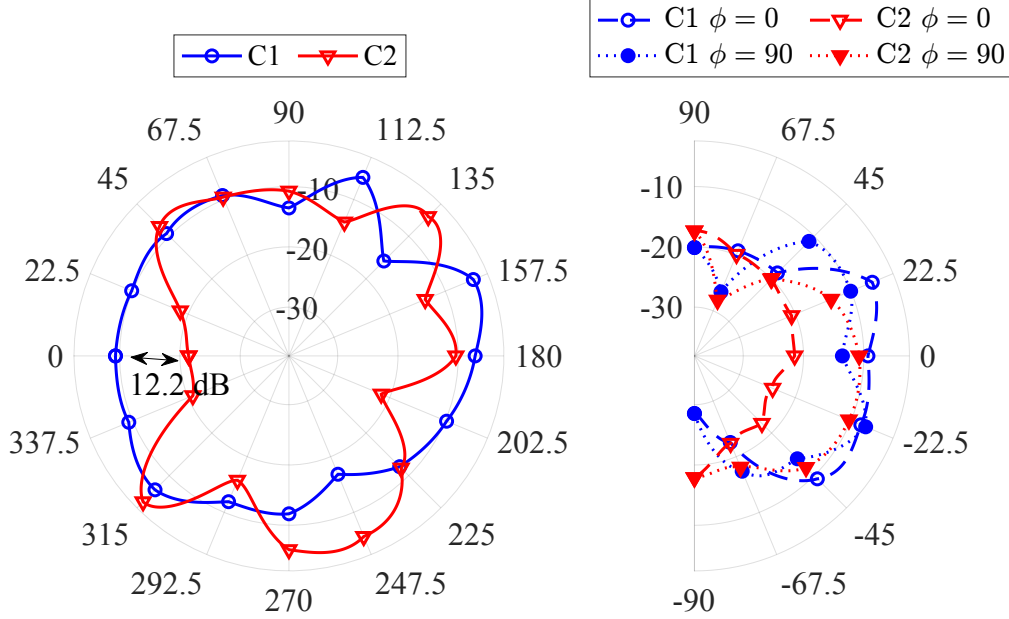


Figure 4.3: Magnitude of the channel between the co-polarized antennas with different body orientations as described in Table 2.1. (left) Variation over azimuth at 0° elevation angle. (right) Variation over elevation angle at azimuth angles 0° and 90° . When the UAV body is parallel with the Tx antenna (C2), the body blocks the LoS path at certain azimuth angles, e.g. 0° .

Table 4.1: Std. Dev. of Co-Polarized Channel over Elevation Angle

	$\phi = 0$	$\phi = 90$
C1	6.5	5.7
C2	1.8	5.3

a 0° elevation angle in the Tx antenna based coordinate system for the two UAV body orientations: perpendicular (left) and parallel (right). The perpendicular case has been studied previously in [25], though the measurements were performed in an anechoic chamber with only the Rx antenna mounted on a UAV. Our in-field results here corroborate the finding that the UAV body reduces the XPD compared to that of an isolated pair of antennas. (The max XPD for the in-field experiments was 11.8 dB compared with 13 dB in the anechoic chamber measurements.) The right side of Fig 4.4 shows that the reduction in XPD, i.e., the increase in the similarity between the co- and cross-polarized channels, does not occur when

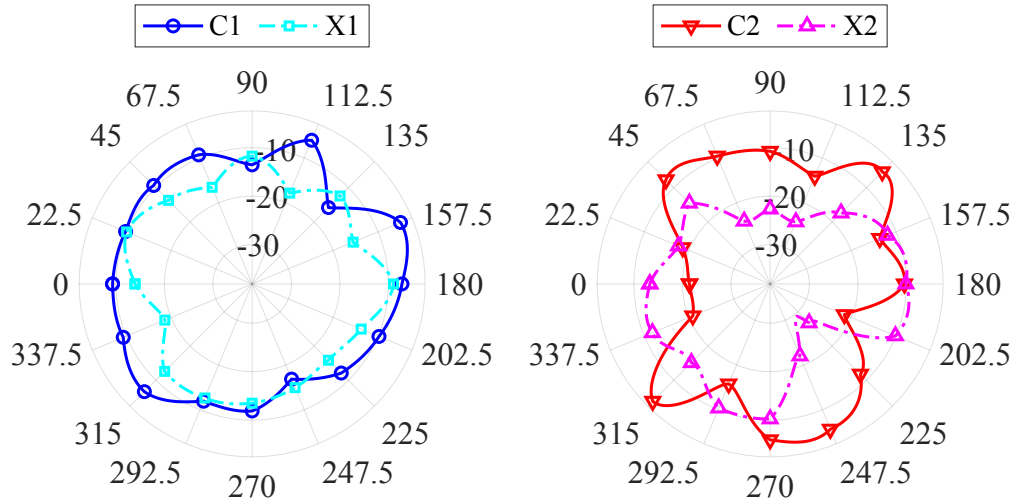


Figure 4.4: Magnitude of the channels between co- and cross-polarized antennas over the azimuth angle for (left) perpendicular and (right) parallel UAV body scenarios as illustrated in Fig. 2.2. The perpendicular UAV body causes polarization mixing, reducing XPD, while the parallel body causes the XPD to vary significantly over the azimuth angle.

the Tx antenna is mounted in parallel with the UAV body. In this case, there is significant difference between the co- and cross-polarized channels (thus variation in XPD) at different azimuth angles.

Table 4.2 presents the statistics of the distribution of the XPD value over the set of all azimuth angles $\{\phi\}$ at 0° elevation for the two different UAV body orientations. Recall that for orientation 1 the UAV bodies are parallel to the Tx antenna (i.e. pairs HH and HV) and for orientation 2 are perpendicular (i.e. VV and VH). For example, the “Max.” column is calculated as

$$\max_{\{\phi\}} \text{XPD}(\phi; \theta = 0).$$

The minimum, mean (μ), and standard deviation (σ) are computed similarly with the exception that μ and σ are computed using the absolute value of the XPD. Note that a negative XPD indicates that the cross-polarized link is stronger than the co-polarized.

The average and standard deviation of the XPD of perpendicular scenario, XPD_2 , are both roughly twice those of the parallel scenario. Additionally, the maximum and minimum XPD_2 are nearly two- and three-times those of XPD_1 , respectively. The takeaway is that while XPD_1 is relatively small and consistent over all azimuth angles, XPD_2 varies

Table 4.2: XPD Statistics over Azimuth Angle ϕ

	Max.	Min.	μ	σ
$\text{XPD}_1 = \text{C1/X1}$	11.8	-3.4	4.0	2.9
$\text{XPD}_2 = \text{C2/X2}$	21.2	-11.4	8.4	5.3

significantly between more extreme values.

The reason for this effect is two-fold and solely due to the orientation of the UAV body. On the one hand, when an antenna is mounted perpendicularly to the UAV body, the body causes enough scattering for polarization mixing to occur which reduces the XPD. On the other hand, when the antenna is mounted parallel to the UAV body, the body induces significant blockages that affect the co- and cross-polarized links differently at different azimuth angles.

4.3 Asymmetric impact of UAV body in 3D Space

In this section, we analyze how the relative position of the UAVs (rather than the orientation of the UAV body with respect to the Tx antenna) affects the distribution of the magnitude of the channel in an asymmetric way. We start by dividing the 3D space around the Tx UAV into two hemispheres, one in front of and one behind the Tx. Specifically, we define the following two sets of points

$$\mathcal{H}_f := \{(\phi, \theta) : 10^\circ < \phi < 170^\circ, |\theta| < 80^\circ\} \quad \text{and}$$

$$\mathcal{H}_b := \{(\phi, \theta) : 190^\circ < \phi < 350^\circ, |\theta| < 80^\circ\}$$

Where $\mathcal{H}_f, \mathcal{H}_b$ are the set of points in 3D space that define the front and behind hemisphere, respectively. We limit the range of the azimuth and elevation angles to emphasize the difference between the two regions—i.e., we do not include points that are close to both hemispheres such as those near the diving line between the front and back hemispheres or those near the poles.

We estimate the distribution of the channel magnitude over all azimuth angles in each hemisphere at each elevation angle as follows: We let H_θ^s be a random variable that represents the channel magnitude $|h|^2$ within hemisphere $s \in \{\mathcal{H}_f, \mathcal{H}_b\}$ at elevation angle θ . Then, we

use kernel density estimation (KDE) to estimate the pdf:

$$\hat{f}_{H_\theta^s}(|h|^2) = \frac{1}{n\beta} \sum_{i=1}^n \Phi \left(\frac{|h|^2 - |h_i|^2}{\beta} \right)$$

where $\hat{f}_{H_\theta^s}(|h|^2)$ is the estimate of the probability density in hemisphere s and elevation angle θ at some channel magnitude $|h|^2$. We use the Gaussian kernel density function Φ with the optimal (under the assumption that the true distribution is Gaussian) bandwidth parameter β [29]. The sum in (4.1) is taken over the n sample values of the channel magnitude $|h_i|^2$. There are $n = 160/0.5 - 1 = 319$ sample values at each elevation angle because the samples span the 160° wide hemisphere at a 0.5° interval following the interpolation. The KDE is computed via the MATLAB function `ksdensity` [30]. Some example of estimated pdfs, $\hat{f}(|h|^2)$ are shown in Fig. 4.5.

Fig. 4.6 shows the sample mean and standard deviation of channel magnitude at each elevation angle θ for both hemispheres. The right y-axis shows the overlapping index [31]:

$$\eta = \int_{|h|^2} \min[\hat{f}_{H_\theta^f}(h), \hat{f}_{H_\theta^b}(h)] dh$$

which is a distance measure between two empirical distributions. When $\eta(A, B) = 1$, it implies that the two distributions A and B are identical, while $\eta(A, B) = 0$ implies that $f_A(x)f_B(x) = 0$ over the support x of A and B , i.e., the distributions are not the same.

Inspecting Fig. 4.6, we make the following three observations:

1) On average, the strongest channel does not occur at $\theta = 0^\circ$ as one would expect based on the radiation pattern of a vertical dipole antenna. Instead, the strongest channel occurs around $\theta = \pm 22.5^\circ$. The sign of θ depends on which hemisphere the Rx is in, i.e.,

$$\arg \max_{\theta} (|h(\theta)|^2) = -22.5^\circ$$

if the Rx is in front and $+22.5^\circ$ if it is behind. This observation leads directly to:

2) The channel magnitude in one hemisphere (either front or behind) is stronger than the other depending on whether the Rx is above or below (with the exception of a few

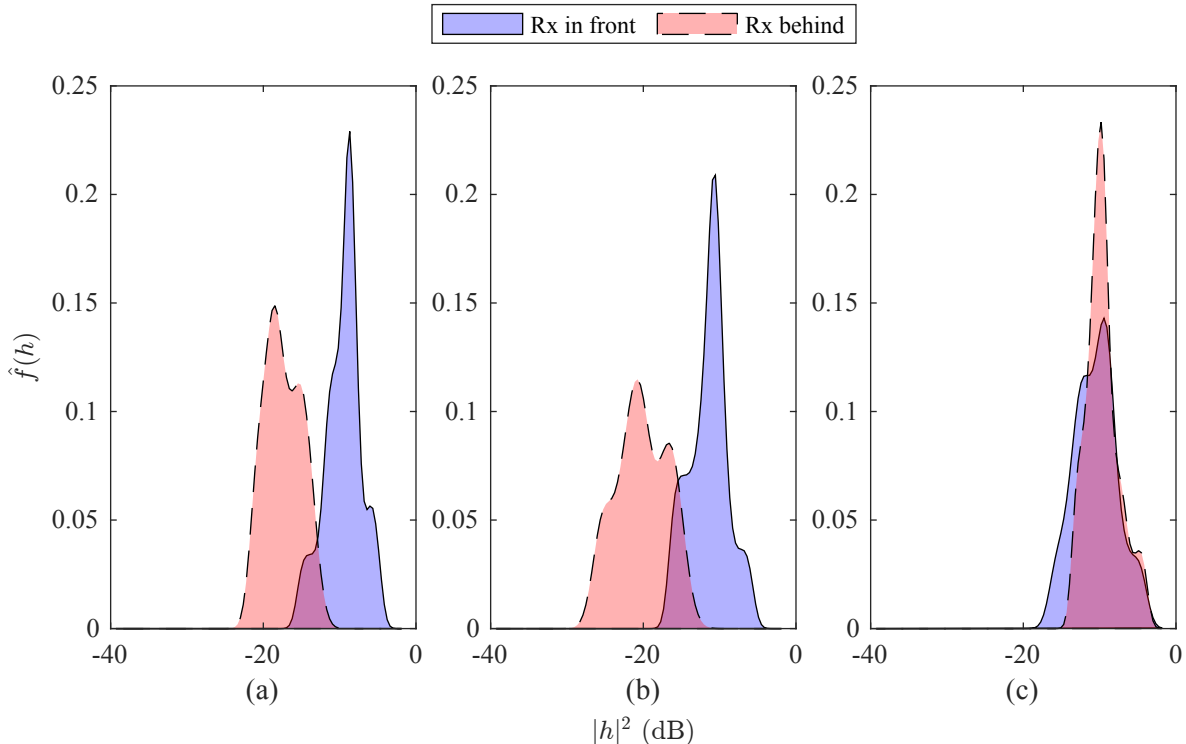


Figure 4.5: Estimated density functions $\hat{f}(|h|^2)$ of the C1 (VV) channel magnitude $|h|^2$ in the front and behind hemispheres at elevation angles (a) $\theta = -30.5^\circ$ (b) $\theta = 43.5^\circ$ and (c) $\theta = 10^\circ$ estimated via Eq. 4.1. The overlap index in (a), (b), and (c) are $\eta = 0.124$, 0.411 , and 0.809 , respectively, which in turn correspond to the minimum η when Rx is below, the minimum η when the Rx is above, and maximum η over all elevation angles.

degrees around 0). The mean channel magnitude in both hemispheres are approximately concave functions over most of the range of the elevation angle, and there is a single cross over point near $\theta = 0^\circ$. This is also contradicts the theoretical channel between two vertical dipole antennas which should not depend on the azimuth angle (which here defines the hemisphere)

3) There is more overlap between the estimated distributions at positive elevation angles than there is at negative angles. This is clear from the shaded regions which represent $\pm\sigma$ around the average channel magnitude, and is also corroborated by the value of η . When $\theta < 0$, i.e., when the Rx is below the Tx, the minimum value of η is 12%, which occurs at $\theta = -30.5^\circ$ and the average is 35%. When the $\theta > 0$ the minimum value of η is only 41% at $\theta = 43.5^\circ$, and the average is 56%. For reference, the maximum value of η is 81% and

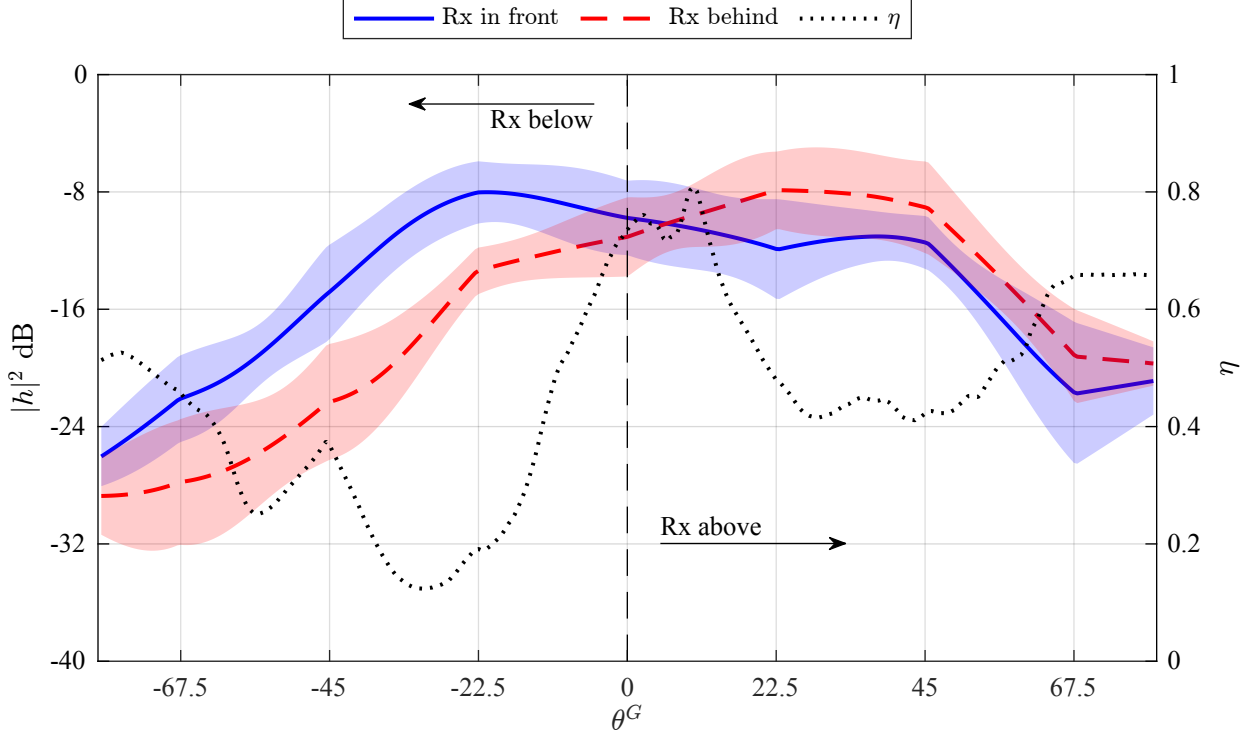


Figure 4.6: Average channel magnitude ($\pm\sigma$) of the of the C1 (VV) channel over azimuth angles where the Rx UAV is in front of or behind the Tx UAV at different UAV based elevation angles θ^G . The value of η is the percentage of overlap between the estimated “in front” and “behind” densities. $\eta = 1$ indicates that the pdf of the two distributions are equal.

occurs at $\theta = 10^\circ$. Fig. 4.5 shows the estimated densities of the two hemispheres at these three elevation angles.

The underlying cause of each of these observations is the UAVs’ bodies and their relative position with respect to one another. One possible reason for the maximum channel to occur at non-zero elevation angles is that at $\pm 22.5^\circ$ either the Tx ($+\theta$) or Rx ($-\theta$) UAV body is positioned in such a way that it can reflect the signal energy towards Rx antenna, forming a directional antenna.

This phenomena also explains why one hemisphere is exclusively stronger depending on the elevation angle. When the Rx is below the Tx: In the front hemisphere, the Rx body acts as a reflector and the Tx body is not in the LoS path; whereas in the behind hemisphere, the Rx body is not in the LoS path and the Tx body is *blocking* the LoS path. These UAV body relationships result in the “below/front” region being stronger than the

“below/behind” region. A similar and reversed relationship exists between the hemispheres for positive elevation angles, where the Tx body can act as a helpful reflector, but the Rx body can only block the signal. The difference between the two “above” regions, however, is smaller than the two “below” as evidenced by the value of η .

The implication of these observations is that UAV bodies create an asymmetry in the behavior of the A2A channel. In other words, the reverse channel magnitude may be greater or weaker than that of the forward channel, despite the theoretical symmetries in the channel due to angular symmetries of the radiation pattern, because the UAV body affects the signal differently depending on whether it is near the Tx or Rx antenna.

4.4 Effect of Position and Antenna Orientation on Capacity

We now demonstrate the effect of the combination of relative drone positioning and antenna orientation on the achievable capacity of the air-to-air channel and show that an antenna selection process can achieve optimal performance.

In the following “globe” figures, each datapoint corresponds to a measurement location described by a (ϕ, θ) pair. Each globe shows the “eastern” hemisphere, i.e. $90^\circ < \phi < 270^\circ$. The location of the datapoint represents the actual location recorded during the experiment, whereas the grid/frame is the intended position. The size and color of each datapoint is proportional to the average capacity over 400 channel estimates at that (ϕ, θ) location.

4.4.1 Fixed Antenna Orientations

Fig. 4.7a shows the average capacity of each measurement location for half of the locations for the VV channel. Notice that the highest capacity values are achieved when the elevation angle is close to 0, i.e. “equator” of the globe. Conversely, for the locations where the vertical displacement is high, i.e. elevation angles close to ± 90 or the “poles”, the average capacity is much lower. There is less dependence on azimuth angle, as expected for a vertically oriented dipole antenna.

Now consider the capacities shown in Fig. 4.7b. As opposed to the VV channel, the highest capacities in the 3D space are found at elevation angles close to $\pm 90^\circ$ (i.e. the “poles” of the globe), while the average capacities of the locations with elevation angle closer to 0 are lower.

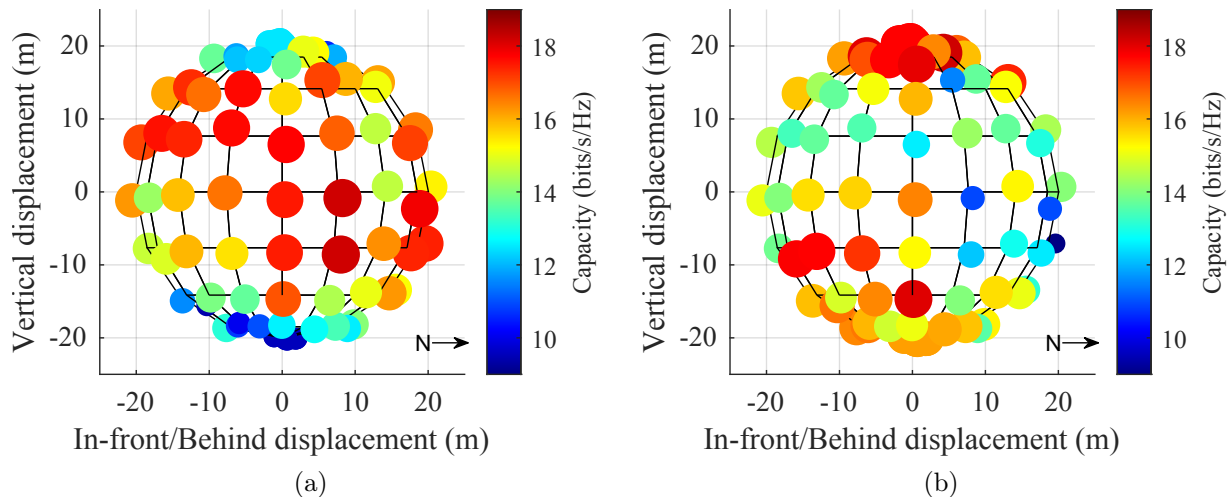


Figure 4.7: Average capacity of the (a) VV and (b) HH TX-RX antenna pairs.

The capacity of the cross-oriented pairs, i.e. HV and VH are shown in Fig. 4.8. Overall the estimated throughput of these pairs is lower than that of the matched pairs VV and HH. This drop in throughput at most locations is due to the misaligned radiation patterns of the two antennas, but there are certain areas which result in higher values.

There are many things that affect the channel in these situations: noise due to UAV motion and vibration, antenna cross- or co-polarization, mismatches or alignments of antenna radiation pattern, and signal blockages or enhancements due to the drone body at either the transmitter or receiver. The result, however, is that the channel has a strong co-dependence on both the relative position of each drone and the orientations of each antenna. Thus in applications where the position of the drones is arbitrary, if the on-board radios are equipped with a single, fixed antenna, the drone-to-drone channel might experience deep fades due only to the changes in relative position.

4.4.2 Best Antenna Pair

Fig. 4.9a shows the transmitter-receiver pair that achieves the highest average capacity at each measurement location. The same patterns as Fig. 4.7 are shown here as well: VV is best around $\theta = 0^\circ$, HH is best around $\theta = \pm 90^\circ$. As noted previously, there are several locations at intermediate elevation angles, where the average measured capacity of the cross-oriented

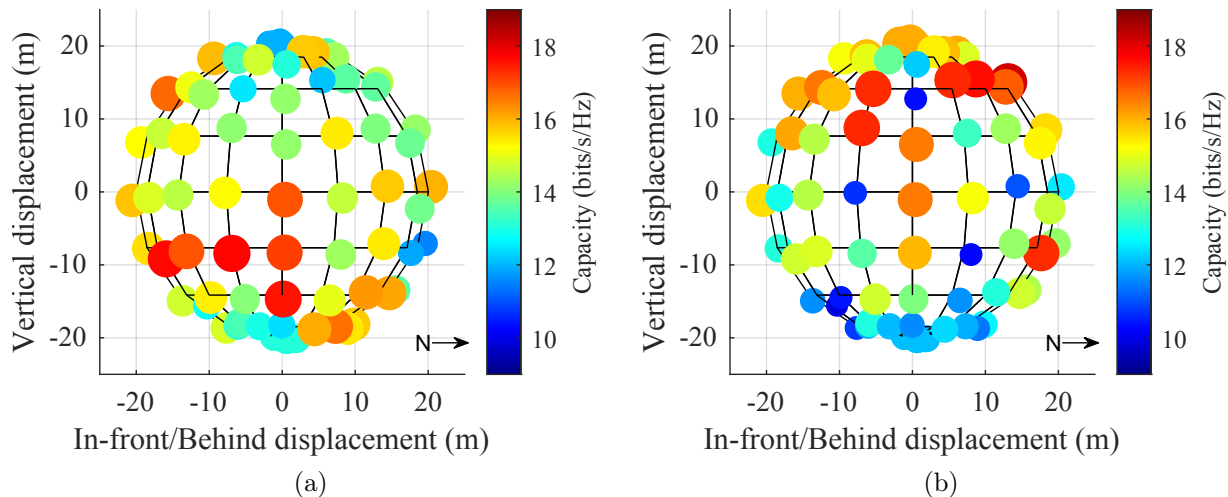


Figure 4.8: (a) Average capacity of the HV and (b) and VH TX-RX antenna pairs.

antenna pairs, VH and HV, is strong, and is in fact the highest of all pairs.

One way to prevent the type of fading events described above could be to outfit both the transmitter and receiver drone with two antennas mounted vertically and horizontally. These antennas could each be connected to a single radio chain through a switch, or to their own radio chain. The transmitter and receiver could then optimally select which of the two antennas to use based on their relative position to one another. In Fig. 4.9b, each capacity datapoint is whichever was highest among the four transmitter-receiver pairs. Notice that the capacity is more or less constant near the highest value at all locations in the 3D space, i.e. we avoid the deep fades observed in the fixed antenna pair scenarios

Fig. 4.10 shows box plots of the measured capacity over all locations which illustrates this result. The middle horizontal line represents the median measured capacity, while the dot shows the mean. The vertical bars depict the total range of the distribution. Outliers (marked with a “+”) are values that lie outside 1.5 times the inter-quartile range (IQR), which is the difference between the 75th and 25th percentile. Perhaps surprisingly, the channel distributions of each antenna pair are largely the same when take over all 3D space. When choosing the optimal antenna pair, the median capacity over all locations in 3D space is over 16 bits/s/Hz which is better than any of the other four fixed pairs, none of which are more than 15 bits/s/Hz; however, the real benefit is in the smaller variance. The IQR for

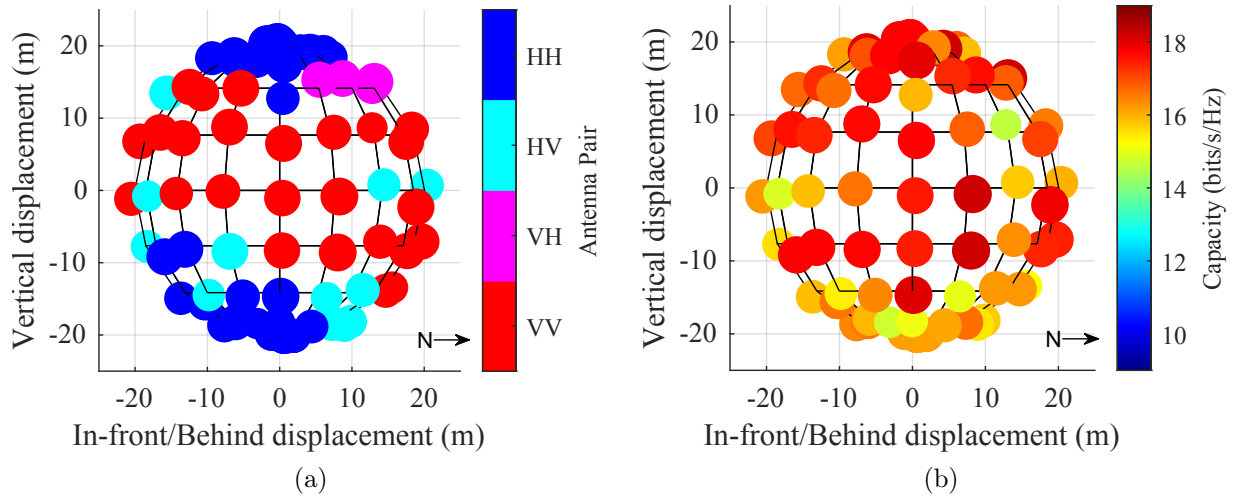


Figure 4.9: (a) Best performing TX-RX antenna pair and (b) its capacity.

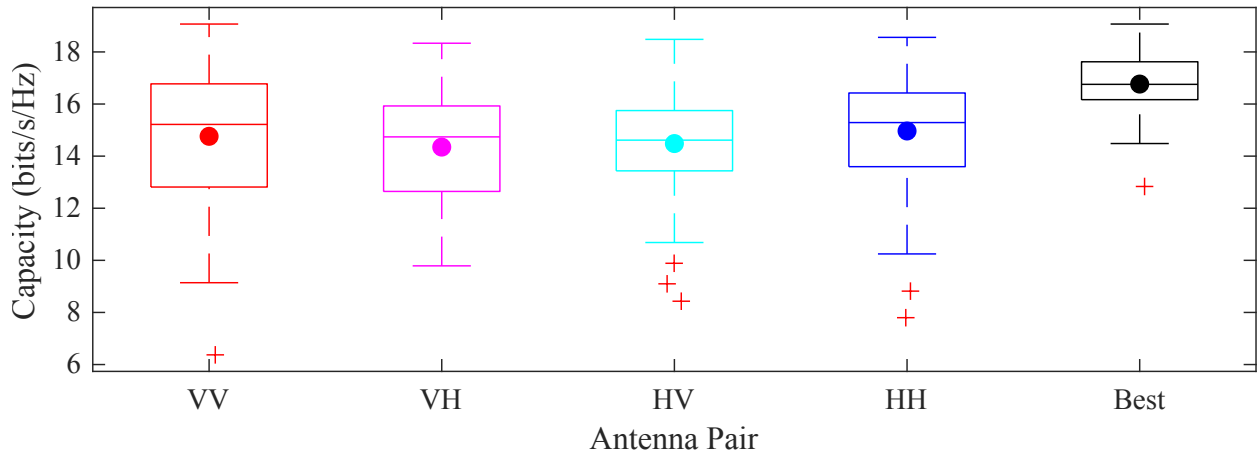


Figure 4.10: Distribution of measured capacity over 3D space of four fixed TX-RX pairs and "best-pair" selection strategy.

the best antenna pair is 2.1 which indicates 50% of the locations were with 1 bits/s/Hz of the median value. The IQRs for the fixed VV, VH, HV, and HH pairs are 3.8, 4.0, 2.9 and 2.8 respectively indicating a larger range of capacity values over the space. Moreover, the lowest capacity measured from the best antenna pair strategy was 12.4 bits/s/Hz while the fixed antenna pairs had much lower capacities at certain locations.

Chapter 5

Conclusions

If the promise of UAVs is to become a reality there must be connectivity between multiple nodes. It is not enough to simply replace the static access point in a wireless system with a mobile version mounted to flying robot. To realize all of these applications, and the others to come, the UAVs must be able to communicate with one another effectively, efficiently, and robustly. This communication is only possible with a thorough understanding of the wireless channel between multiple UAVs, and since the power of the UAV comes from its positional flexibility, we must understand the channel from every angle.

In this work we have begun to approach this complete view of the 3D wireless air-to-air channel through real-world measurements. Our experiment was designed to isolate two variables in the this channel: the arbitrary position of the Rx UAV relative to a fixed Tx, and the location and orientation of a dipole antenna at either end. Conducting field measurements with UAVs is difficult as environmental conditions are variable and the UAV location is never static—the act of hovering always introduces some movement and variation in the channel—but we have done our best to conduct a controlled, repeatable experiment and have demonstrated the reliability of the results.

A potential shortcoming of this work is that it focuses on too narrow a scenario. While true we used only one type of drone, one type of antenna, and a relatively simple channel sounding method, we do not claim that the specific values presented here or even the general patterns of the channel in 3D space will apply to every scenario. They surely will vary with different antenna types and placements and with different UAV form-factors and build materials. Rather, the point of this work is to demonstrate the need for A2A measurements by showing the variability in this channel even for the narrow scenario presented in this experiment. That the strength of a wireless channel between a Tx and Rx depends on the orientation of the antenna and the structures interfering in the line-of-sight path is obvious,

but the specific ways in which these two variables work together to effect the A2A channel is anything but. If we are to model, and one day build, systems of large numbers of UAVs, its critical to have solid data and a solid understanding of the channels between the nodes. This work represents a first step towards this future.

BIBLIOGRAPHY

- [1] H. Magazine, “Emergency-response drones to save lives in the digital skies,” Jun. 2022, library Catalog: horizon.scienceblog.com. [Online]. Available: <https://horizon.scienceblog.com/2073/emergency-response-drones-to-save-lives-in-the-digital-skies/> 1
- [2] Scott Howe, “Drone Delivery for Healthcare and Emergency Service Providers,” Jul. 2022, library Catalog: www.commercialuavnews.com. [Online]. Available: <https://www.commercialuavnews.com/drone-delivery/drone-delivery-for-healthcare-and-emergency-service-providers> 1
- [3] —, “AT&T’s Flying COW Transmits 5G Network by Tethered Drone,” Jun. 2022, library Catalog: www.commercialuavnews.com. [Online]. Available: <https://www.commercialuavnews.com/public-safety/at-t-s-flying-cow-transmits-5g-network-by-tethered-drone> 1
- [4] Greg Nichols, “How cell tower ‘COW’ drones will keep fans safe at the Super Bowl,” Feb. 2022, library Catalog: www.zdnet.com. [Online]. Available: <https://www.zdnet.com/home-and-office/networking/how-cell-tower-cow-drones-will-keep-fans-safe-at-the-super-bowl/> 1
- [5] A. Mairaj, A. I. Baba, and A. Y. Javaid, “Application Specific Drone Simulators: Recent Advances and Challenges,” *Simulation Modelling Practice and Theory*, vol. 94, pp. 100–117, Jul. 2019, arXiv: 1902.00616. [Online]. Available: <http://arxiv.org/abs/1902.00616> 2
- [6] S. Baidya, Z. Shaikh, and M. Levorato, “FlyNetSim: An Open Source Synchronized UAV Network Simulator based on ns-3 and Ardupilot,” in *Proceedings of the 21st ACM International Conference on Modeling, Analysis and Simulation of Wireless and Mobile Systems*, ser. MSWIM ’18. New York, NY, USA: Association for Computing Machinery, Oct. 2018, pp. 37–45. [Online]. Available: <https://doi.org/10.1145/3242102.3242118> 2
- [7] A. A. Khuwaja, Y. Chen, N. Zhao, M. Alouini, and P. Dobbins, “A Survey of Channel Modeling for UAV Communications,” *IEEE Communications Surveys Tutorials*, vol. 20, no. 4, pp. 2804–2821, 2018. 2
- [8] W. Khawaja, I. Guvenc, D. W. Matolak, U. Fiebig, and N. Schneckenburger, “A Survey of Air-to-Ground Propagation Channel Modeling for Unmanned Aerial Vehicles,” *IEEE Communications Surveys Tutorials*, vol. 21, no. 3, pp. 2361–2391, 2019. 2

- [9] R. Sun, D. W. Matolak, and W. Rayess, “Air-Ground Channel Characterization for Unmanned Aircraft Systems—Part IV: Airframe Shadowing,” *IEEE Transactions on Vehicular Technology*, vol. 66, no. 9, pp. 7643–7652, Sep. 2017. [2](#), [3](#)
- [10] J. Kunisch, I. d. l. Torre, A. Winkelmann, M. Eube, and T. Fuss, “Wideband time-variant air-to-ground radio channel measurements at 5 GHz,” in *Proceedings of the 5th European Conference on Antennas and Propagation (EUCAP)*, Apr. 2011, pp. 1386–1390, iSSN: 2164-3342. [2](#), [3](#)
- [11] J. Chen, D. Raye, W. Khawaja, P. Sinha, and I. Guvenc, “Impact of 3D UWB Antenna Radiation Pattern on Air-to-Ground Drone Connectivity,” in *2018 IEEE 88th Vehicular Technology Conference (VTC-Fall)*, Aug. 2018, pp. 1–5, iSSN: 2577-2465. [2](#), [3](#)
- [12] W. Khawaja, O. Ozdemir, F. Erden, I. Guvenc, and D. W. Matolak, “UWB Air-to-Ground Propagation Channel Measurements and Modeling Using UAVs,” in *2019 IEEE Aerospace Conference*, Mar. 2019, pp. 1–10, iSSN: 1095-323X. [2](#), [3](#)
- [13] W. Khawaja, O. Ozdemir, and I. Guvenc, “Temporal and Spatial Characteristics of mm Wave Propagation Channels for UAVs,” in *2018 11th Global Symposium on Millimeter Waves (GSMM)*, May 2018, pp. 1–6. [2](#), [3](#)
- [14] —, “UAV Air-to-Ground Channel Characterization for mmWave Systems,” in *2017 IEEE 86th Vehicular Technology Conference (VTC-Fall)*, Sep. 2017, pp. 1–5. [2](#), [3](#)
- [15] J. Romeu, A. Aguiasca, J. Alonso, S. Blanch, and R. R. Martins, “Small UAV radiocommunication channel characterization,” in *Proceedings of the Fourth European Conference on Antennas and Propagation*, Apr. 2010, pp. 1–5, iSSN: 2164-3342. [2](#), [3](#)
- [16] T. Tavares, P. Sebastião, N. Souto, F. J. Velez, F. Cercas, M. Ribeiro, and A. Correia, “Generalized LUI Propagation Model for UAVs Communications Using Terrestrial Cellular Networks,” in *2015 IEEE 82nd Vehicular Technology Conference (VTC2015-Fall)*, Sep. 2015, pp. 1–6. [2](#), [3](#)
- [17] C. Cheng, P. Hsiao, H. T. Kung, and D. Vlah, “Performance Measurement of 802.11a Wireless Links from UAV to Ground Nodes with Various Antenna Orientations,” in *Proceedings of 15th International Conference on Computer Communications and Networks*, Oct. 2006, pp. 303–308, iSSN: 1095-2055. [2](#), [3](#)
- [18] E. Yanmaz, R. Kuschnig, and C. Bettstetter, “Channel measurements over 802.11a-based UAV-to-ground links,” in *2011 IEEE GLOBECOM Workshops (GC Wkshps)*, Dec. 2011, pp. 1280–1284, iSSN: 2166-0077. [2](#), [3](#)
- [19] —, “Achieving air-ground communications in 802.11 networks with three-dimensional aerial mobility,” in *2013 Proceedings IEEE INFOCOM*, Apr. 2013, pp. 120–124, iSSN: 0743-166X. [2](#), [3](#)

- [20] N. Ahmed, S. S. Kanhere, and S. Jha, “On the importance of link characterization for aerial wireless sensor networks,” *IEEE Communications Magazine*, vol. 54, no. 5, pp. 52–57, May 2016. 2, 3
- [21] J. Allred, A. B. Hasan, S. Panichsakul, W. Pisano, P. Gray, J. Huang, R. Han, D. Lawrence, and K. Mohseni, “SensorFlock: an airborne wireless sensor network of micro-air vehicles,” in *Proceedings of the 5th international conference on Embedded networked sensor systems*, ser. SenSys ’07. New York, NY, USA: Association for Computing Machinery, Nov. 2007, pp. 117–129. [Online]. Available: <https://doi.org/10.1145/1322263.1322275> 3
- [22] A. Shaw and K. Mohseni, “A Fluid Dynamic Based Coordination of a Wireless Sensor Network of Unmanned Aerial Vehicles: 3-D Simulation and Wireless Communication Characterization,” *IEEE Sensors Journal*, vol. 11, no. 3, pp. 722–736, Mar. 2011. 3
- [23] N. Goddemeier and C. Wietfeld, “Investigation of Air-to-Air Channel Characteristics and a UAV Specific Extension to the Rice Model,” in *2015 IEEE Globecom Workshops (GC Wkshps)*. San Diego, CA, USA: IEEE, Dec. 2015. 3
- [24] M. Badi, J. Wensowitch, D. Rajan, and J. Camp, “Experimental Evaluation of Antenna Polarization and Elevation Effects on Drone Communications,” in *Proceedings of the 22nd International ACM Conference on Modeling, Analysis and Simulation of Wireless and Mobile Systems*, ser. MSWIM ’19. New York, NY, USA: Association for Computing Machinery, Nov. 2019, pp. 211–220. 3
- [25] —, “Experimentally Analyzing Diverse Antenna Placements and Orientations for UAV Communications,” *IEEE Transactions on Vehicular Technology*, vol. 69, no. 12, pp. 14989–15004, Dec. 2020. 3, 13, 18
- [26] C. A. Balanis, *Antenna theory: analysis and design*, 4th ed. Hoboken: Wiley, 2016. 11
- [27] D. Tse and P. Viswanath, *Fundamentals of Wireless Communication*, 1st ed. Cambridge University Press, May 2005. [Online]. Available: <https://www.cambridge.org/core/product/identifier/9780511807213/type/book> 12
- [28] I. Amidror, “Scattered Data Interpolation Methods for Electronic Imaging Systems: A Survey,” 2002. 16
- [29] B. W. Silverman, *Density estimation for statistics and data analysis*, ser. Monographs on statistics and applied probability. Boca Raton: Chapman & Hall/CRC, 1998, no. 26. 21
- [30] MathWorks, “Kernel smoothing function estimate for univariate and bivariate data - MATLAB ksdensity.” [Online]. Available: <https://www.mathworks.com/help/stats/ksdensity.html> 21
- [31] T. E. Clemons and E. L. Bradley, “A nonparametric measure of the overlapping coefficient,” *Computational Statistics & Data Analysis*, vol. 34, no. 1, pp. 51–61, Jul. 2000. 21